Journal Pre-proof

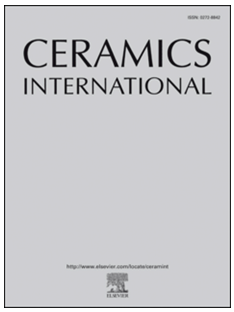

Dry sliding wear behavior of in situ Ti6Al4V/TiN composites 3D manufactured by Laser-Directed Energy Deposition

C. Sánchez de Rojas Candela, A. Riquelme, P. Rodrigo, B. Torres, J. Rams

PII: S0272-8842(25)02626-4

DOI: https://doi.org/10.1016/j.ceramint.2025.06.002

Reference: CERI 47216

To appear in: *Ceramics International*

Received Date: 14 February 2025

Revised Date: 21 May 2025

Accepted Date: 1 June 2025

Please cite this article as: C. Sánchez de Rojas Candela, A. Riquelme, P. Rodrigo, B. Torres, J. Rams, Dry sliding wear behavior of in situ Ti6Al4V/TiN composites 3D manufactured by Laser-Directed Energy Deposition, *Ceramics International*, https://doi.org/10.1016/j.ceramint.2025.06.002.

This is a PDF file of an article that has undergone enhancements after acceptance, such as the addition of a cover page and metadata, and formatting for readability, but it is not yet the definitive version of record. This version will undergo additional copyediting, typesetting and review before it is published in its final form, but we are providing this version to give early visibility of the article. Please note that, during the production process, errors may be discovered which could affect the content, and all legal disclaimers that apply to the journal pertain.

© 2025 Published by Elsevier Ltd.

Journal Pre-proof

Dry sliding wear behavior of in situ Ti6Al4V/TiN composites 3D manufactured by Laser-Directed Energy Deposition

C. Sánchez de Rojas Candela*[1]; A. Riquelme[1]; P. Rodrigo[1]; B. Torres[1]; J. Rams[1]

* Corresponding author. E-mail address: carmen.srojascandela@urjc.es

[1] Materials Science and Engineering Group, Universidad Rey Juan Carlos, Madrid 28933, Spain

Abstract

In this work, the wear behavior of Ti6Al4V/TiN composites additively manufactured by laser-directed energy deposition has been studied. The substitution of argon for nitrogen created a reactive atmosphere during the fabrication process, triggering a direct reaction between the molten Ti6Al4V and the nitrogen molecules, creating in situ TiN ceramic reinforcement within the Ti6Al4V metal matrix. The effect of fabrication parameters, such as laser power and scanning speed, on the wear resistance of the different samples was evaluated and compared with the unreinforced base material, which was manufactured under argon. Samples were classified according to heat input: 37.5, 75, 95, and 190 J/mm. Wear tests were performed using a pin-on-disc configuration, employing 316L stainless steel as the counterbody material. The observed wear mechanisms were subsequently identified based on the test results. The influence of microstructure and microhardness on the coefficient of friction, mass loss of pins and counterbodies, and wear rate of each material was also evaluated. The percentage and distribution of the reinforcement generated during fabrication depended on the percentage of nitrogen diffusing into the titanium, which was intrinsically linked to the fabrication parameters. The nitrogen uptake increased with higher heat input, thereby affecting the wear rates and wear mechanisms. The measured Ti6Al4V/TiN Vickers microhardness was double that of the unreinforced samples, although this trend decreased at higher laser power. The Ti6Al4V/TiN sample manufactured with a heat input of 75 J/mm exhibited the highest microhardness (1300 HV2). The formation of TiN reinforcement led to reduced pin mass losses and wear rates, as well as increased coefficients of friction. The Ti6Al4V/TiN samples fabricated at 37.5 and 95 J/mm exhibited the lowest wear rates (2,5 x 10^{-13} m^3/Nm). An abrasive wear mechanism was observed in all Ti6Al4V/TiN samples, predominating when the laser scanning speed was lower (75 and 190 J/mm), due to greater nitride phase formation, which enhanced hardness. This mechanism combined with an oxidative component at a heat input of 190 J/mm, where a mechanically mixed layer was formed, while combining with an adhesive wear mechanism at higher scanning speeds (37.5 and 95 J/mm).

Keywords: dry sliding wear behavior, laser-directed energy deposition, additive manufacturing, in situ Ti6Al4V/TiN composites, nitriding reaction

Journal Pre-proof

1. Introduction

Additive manufacturing (AM) is a fabrication method that offers several advantages, such as design flexibility (including the ability to produce complex geometries), reduced material waste and fewer fabrication steps, the capability to repair metallic components, and the possibility to alter the processing atmosphere, which makes it increasingly widely used [1,2]. Laser-directed energy deposition (L-DED) is an AM technique where a laser beam melts material (either powder or wire) and deposits it onto a substrate to form the first layer, continuing layer-by-layer following a computer-aided design (CAD) model [3]. This AM method is gaining significant interest for the production of metallic materials such as titanium, steel, nickel, and aluminum alloys [4,5].

During the L-DED process, argon is commonly used to protect 3D-printed parts from oxidation. However, nitrogen has also been used as a shielding gas in place of argon by researchers studying its effect on the microstructure and mechanical properties of 316L stainless steel [1]. The direct reaction between nitrogen molecules in the atmosphere and titanium melted by the laser beam leads to the formation of titanium nitride phases within the titanium matrix, resulting in an in situ fabricated metal matrix composite (MMC) [6,7]. This novel reinforcement method results in a clean and strong matrix–reinforcement interface, enhancing the microhardness and abrasive resistance of the composite material [8].

In addition, the fabrication parameters in AM have a strong influence on the final properties of printed parts [9]. Parameters such as laser power, laser scanning speed, hatch distance, gas flow rate, and powder feed rate can be adjusted to optimize both the manufacturing process and the final properties of the material [9–11]. For instance, laser power and scanning speed affect the microstructure and heat-affected zone (HAZ) since the heat input, peak temperatures, and cooling rates vary [12,13]. A. Riquelme et al. [14] modified laser power and scanning speed to study its effect on the in situ fabrication of Al/AlN samples by L-DED and developed a process map for porosity and part dimensions as a function of the processing parameters. Y. Liu et al. [15] tuned the laser power, scanning speed, and feed rate during laser melting deposition (LMD) manufacturing of in situ (TiC+Ti_5Si_3)/Ti6Al4V composites and determined the optimal combination by studying their microstructure, hardness, and friction behavior.

MMCs consist of at least two constituents: a metallic matrix and a reinforcement material such as ceramics or organic compounds [16,17]. Ti6Al4V alloy is one of the most utilized materials in AM owing to its low thermal conductivity, light weight, good structural stability, great resistance to corrosion, and high elastic limit. However, its low wear resistance makes it one of the most commonly reinforced alloys [18,19]. Meanwhile, reinforcement materials such as carbides, nitrides, and oxides have been

utilized to optimize the properties of base alloys and make them more attractive for automotive, aerospace, and several other applications [20]. Accordingly, reinforcements such as titanium nitride can improve the wear behavior of matrices such as Ti6Al4V, forming MMCs with combined microstructures and enhanced mechanical properties. While MMC fabrication is possible through conventional routes, their production via AM remains a challenge for current research efforts [17].

MMCs are able to perform remarkably well in terms of wear behavior compared to the main alloy [21]. In situ MMCs, in particular, exhibit better quality interfaces than ex-situ MMCs, leading to significantly improved wear behavior since the reinforcement is less likely to detach from the matrix material due to the generated friction [22].

To study the tribological properties of Ti–TiN composites, J. Umeda et al. [23] manufactured Ti composites with ring-shaped dispersoids by premixing powders and heat treating them under nitrogen gas and evaluated their wear behavior. The coefficient of friction (CoF) decreased for the composites and was more stable compared to pure Ti due to their higher microhardness and the appearance of an abrasive wear mechanism. C. Song et al.[24] used plasma spray–physical vapor deposition to synthesize in situ TiN coatings on Ti6Al4V substrates, which altered the microstructure and enhanced the mechanical properties of the base material. Utilizing laser AM, W. Wei et al. [25] developed a novel method for in situ synthesis of TiN and AlN Ti6Al4V matrix composites that presented higher microhardness, compressive yield strength, and ultimate compressive strength with increasing nitrogen content. B. AlMangour et al. [26] processed in situ TiC particles within 316L stainless steel by selective laser melting (SLM) and studied the effect of laser energy density on the densification, microstructure, and mechanical properties of the materials.

However, there is limited literature on the influence of L-DED processing parameters on the wear behavior of in situ Ti–TiN composites. This study investigates the effect of different laser powers (1200–700 and 650–100 W) and laser scanning speeds (5 and 10 mm/s) on the wear behavior of L-DED-manufactured titanium matrix composites containing in situ synthesized TiN. The relationships among microstructure, microhardness, wear rate, CoF, pin and disc mass losses, and wear mechanisms are examined.

2. Materials and methods

Ti6Al4V alloy powder was used to manufacture in situ Ti/TiN composite samples with thin wall geometry and dimensions of 60 × 15 mm^2 using L-DED. The spherical morphology and size distribution (9–32 μm) of the Ti6Al4V particles are shown in Figures

1a and 1b, respectively. The powder was kept at room temperature and delivered through a Fraunhofer IWS COAX 8 coaxial nozzle, sprayed coaxially at a 5 g/min feed rate, with the laser focused 12.5 mm below the nozzle tip.

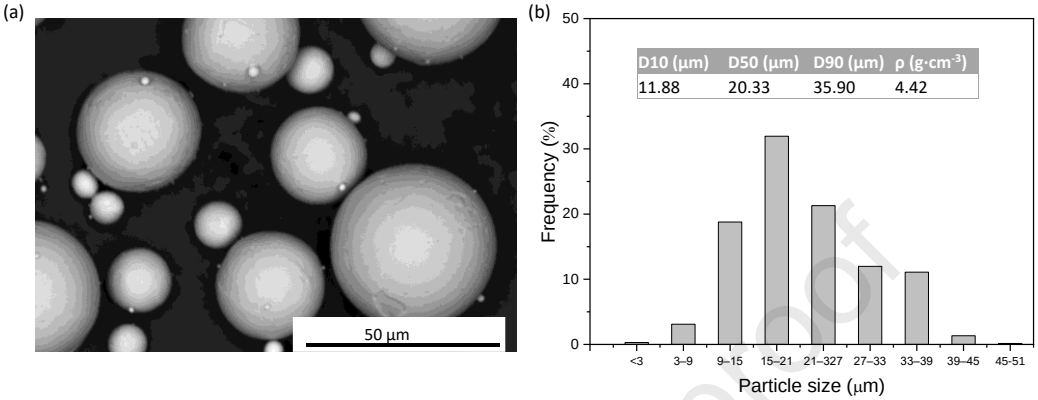

Figure 1. (a) SEM micrograph of Ti6Al4V feed powder particles; (b) particle size distribution of the Ti6Al4V powder.

The support bases were made of 316L sheets (100 × 100 × 20 mm^3) and were heated to 150 ˚C using a hot plate to prevent potential thermal shock. The L-DED system was equipped with an ABB IRB2400 robot and a high-power ROFIN diode laser (DL013S) operating at 1300 W with an 808–940 nm wavelength. The laser power was adjusted for different samples, with two configurations: 1200 W of initial power reduced to 700 W and 650 W reduced to 100 W, to mitigate heat buildup. Argon was used as the carrying and protective gas, while nitrogen served as the reactive gas, supplied at a pressure of 4.5 atm and a flow rate of 0.05 L/s. The set of parameters used for manufacturing under the two atmospheric conditions (inert and reactive) are listed in Table 1. Laser power (W) and scanning speed (mm/s) were varied, leading to eight different conditions for wear resistance analysis. Three specimens were fabricated for each set of manufacturing parameters to ensure the repeatability of the experimental results and minimize variability.

Table 1. Set of parameters for the different sample conditions

Condition	Initial Laser power (W)	Final Laser Power (W)	Scanning speed (mm/s)	Carrying gas	Abbreviated name
C1	650	100	5	Argon	650-5-Ar
C2	650	100	10	Argon	650-10-Ar
C3	1200	700	5	Argon	1200-5-Ar

C4	1200	700	10	Argon	1200-10-Ar
C5	650	100	5	Nitrogen	650-5-N
C6	650	100	10	Nitrogen	650-10-N
C7	1200	700	5	Nitrogen	1200-5-N
C8	1200	700	10	Nitrogen	1200-10-N

To study the microstructure and measure the Vickers microhardness of the different manufactured samples, they were prepared for metallographic analysis: cut crosswise, mounted in a conductive resin, wet ground with silicon carbide paper down to 4000 grit, and polished with a 1 µm diamond paste.

Microhardness was measured using a Vickers pyramid indenter with a Shimadzu microhardness tester, applying a 19.6 N load for 10 s (HV2). A minimum of fifteen indentations spaced 1000 µm apart were performed on each sample, and testing was performed in triplicate.

A Microtest MT/10/SCM tribometer was used under dry sliding conditions. The testing parameters were a **200 rpm speed**, **5 N load**, **10 mm wear track diameter**, and **1000 m total wear distance**. The samples were cut into 15 x 2 x 2 mm^3 pins, which were mechanically clamped into a sample holder. The counterbody was a 30 × 30 mm 316L stainless steel sheet (240 HV hardness). This alloy, having a different composition from the test material, facilitated the identification of the adhesive wear mechanism. For each experimental condition, error analysis was conducted based on the results from the three repeated wear tests. Standard deviations were calculated for each measured parameter, including mass loss, CoF, and wear rate, to estimate the experimental uncertainty of each condition.

All samples (both pins and counterbodies) were weighed before and after the wear tests with a Sartorius BP 211S balance with a precision of ± 0.0001 g to determine mass loss. Volume loss was calculated from the measured mass loss (before and after the wear test) and the material density. The wear coefficient was calculated using the Lancaster equation [27]:

$$K = \frac{V}{W\,L} \qquad \text{(Eq. 1)}$$

where K is the wear coefficient (mm^3/(N m)), V is the wear volume (mm^3), W is the applied normal load (N), and L is the sliding distance (m).

Scanning electron microscopy (SEM; Hitachi S-3400N) was used to determine the microstructure and wear mechanisms of the tested materials; the scanning electron

171 microscope was equipped with an energy dispersive X-ray spectrometer (EDS) for
172 elemental analysis. Image analysis software—Leica Application Suite, SemAfore, and
173 ImageJ—was utilized to process and analyze the SEM micrographs.
174
175 **2.1. Heat Input**
176 The heat input (J/mm) relates the laser power (W) to the laser scanning speed (mm/s)
177 and defines the amount of heat the sample is exposed to during the AM process
178 (Equation 2) [28].

179
180 $$\textit{Heat Input (J/mm)} = \frac{laser\ power\ (W)}{scanning\ speed\ (^{mm}/_{s})} \qquad \text{(Eq. 2)}$$

181
182 The calculated heat input values corresponding to the different manufacturing
183 parameters are presented in Table 2. From this point forward, the samples are referred
184 to according to the associated heat input value generated during their fabrication.
185
186 *Table 2. Heat input for the sample conditions used in this research.*

Initial Laser power (W)	Scanning speed (mm/s)	Conditions	Heat Input (J/mm)
650	10	C2, C6	37,5
650	5	C1, C5	75
1200	10	C4, C8	95
1200	5	C3, C7	190

187
188 **3. Results and discussion**

189 **3.1. Microstructural analysis of the samples**

190 The microstructures of the L-DED manufactured samples were studied using SEM.
191 Micrographs of unreinforced titanium at the top part of the sample are shown in Figure
192 2. An extended study of the microstructure and mechanical properties of these samples
193 has already been published by the present authors [7]. All the samples exhibited a
194 Widmanstätten alpha–beta titanium microstructure due to the decomposition of α´
195 martensite at relatively slow cooling rates. The alpha (α) phase appeared as elongated
196 grains (dark gray in the image), while the beta (β) phase formed in the intergranular
197 zones (light gray). During the L-DED process, high temperatures combined with relatively
198 low cooling rates, leading to the transformation of α' martensite towards the
199 equilibrium α + β microstructure. Fluctuations in the supplied heat input during the
200 process, due to changes in manufacturing parameters, did not result in significant
201 microstructural variations. This could be attributed to accumulated heat during the
202 production of subsequent layers, which hindered microstructural changes in certain

areas. However, as the supplied heat input increased, the microstructure slightly shifted to a coarser lamellar structure due to the slower cooling rate, resulting in greater reheating from prolonged exposure to high temperatures and allowing the growth of wider α-phase needles and the formation of wider intergranular β regions. The lamellar width increased with heat input, ranging from 3.5 ± 0.8 µm (37.5 J/mm) to 6.1 ± 1.1 µm (190 J/mm), with intermediate values of 4.7 ± 1.1 µm (75 J/mm) and 5.4 ± 1.8 µm (95 J/mm). Thus, samples manufactured with greater heat input exhibited wider and less refined microstructures, which in turn reduced hardness due to the presence of thicker α plates and a larger amount of β phase, offering fewer barriers to dislocation motion [29]. Because Ti6Al4V has low thermal conductivity, heat dissipation through the previously deposited layers was limited, leading to a slow cooling rate.

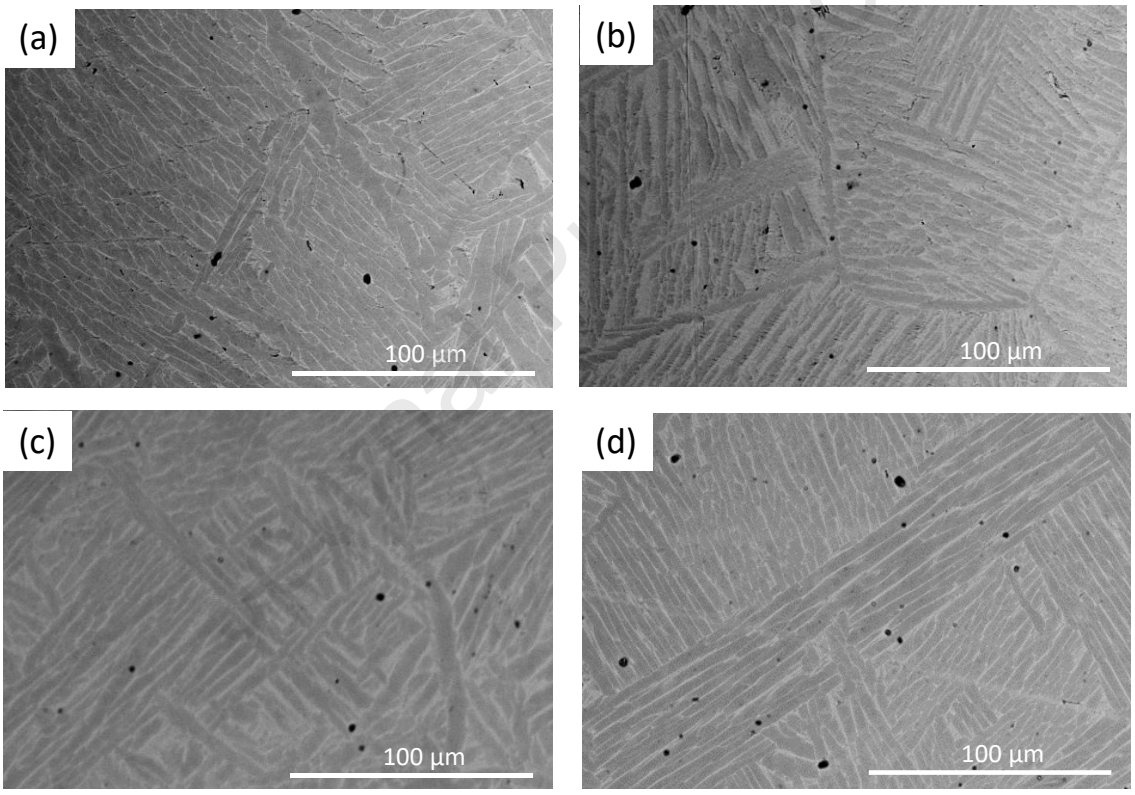

Figure 2. SEM micrographs of the Ti microstructures in the top region of the cross sections corresponding to heat inputs of (a) 37.5, (b) 75, (c) 95, and (d) 190 J/mm.

The microstructure of the L-DED Ti–TiN composites in the top region of the cross-section is shown in Figure 3. Although the microstructure varied with heat input, an alpha–beta titanium matrix was consistently present in all cases. In addition, TiN and Ti_2N dendrites were formed as in situ reinforcements through the reaction between nitrogen molecules in the reactive atmosphere and molten titanium [7].

Figure 3a reveals the microstructure of the 37.5 J/mm sample, composed of a titanium matrix with an Al-rich region (α phase) around a V-rich zone (β phase) with TiN dendrites

exhibiting high interdendritic porosity. Ti_2N appeared as a minority phase, formed depending on the nitrogen content and cooling rate. A higher distribution of TiN dendrites was observed when the laser power was 650 W and the scanning speed was reduced, corresponding to a heat input of 75 J/mm (Figure 3b). At a higher laser power of 1200 W and increased scanning speed corresponding to a heat input of 95 J/mm, TiN dendrites appeared in circular patterns (Figure 3c), where three different reaction mechanisms occurred. The outer ring consisted of TiN and eutectoid α-Ti–Ti_2N dendrites in a titanium matrix (area 1, orange). Inside this ring, a second, thinner ring was formed with an α-Ti phase matrix, TiN dendrites, and Ti_2N (area 2, green). The last ring was situated inside the other two and presented primary dendrites of α-Ti and α + β phases (area 3, blue). This sample exhibited a Ti_2N XRD peak with higher intensity than those of other samples. While Ti_2N is less hard than TiN, it typically exhibits better adhesion to the Ti6Al4V matrix, likely due to accelerated thermal cycles and enhanced nitrogen diffusion into the molten titanium [30]. The microstructure of the 190 J/mm sample (Figure 3d) was similar to that of the 95 J/mm sample but showed a smaller V-rich region due to the slower scanning speed.

Overall, dendrite distribution and size varied with the heat input. Specifically, lower laser scanning speeds increased TiN dendrite formation and enhanced its distribution due to elevated temperatures that facilitated the in situ reaction. Furthermore, scanning speed and laser power had different effects on the microstructure: when the laser power was held constant, the dendrite size and distribution were higher for slower scanning speeds owing to higher heat input and slower cooling rates, as observed when comparing Figures 3a and 3b and 3c and 3d. Nevertheless, when the laser scanning speed was held constant, an increase in laser power also increased TiN dendrite distribution, as observed when comparing Figures 3b and 3d and 3a and 3c. These observations are consistent with the XRD peaks discussed in a previously published article by the present authors [7].

Figures 3e–h present detailed microstructural and elemental analyses for the 37.5 (Figures 3e and 3f) and 75 J/mm (Figures 3g and 3h) samples. These results confirm the influence of scanning speed on the extent of nitriding in the titanium metallic matrix. Lower scanning speeds (corresponding to a heat input of 75 J/mm) resulted in a significantly increased formation of TiN within the samples. This was evident from the elemental distribution of aluminum (shown in dark blue) and nitrogen (in green), since aluminum is primarily associated with the titanium matrix (α-phase), whereas nitrogen is found in the reinforcement phase, where it combines with titanium to form titanium nitrides.

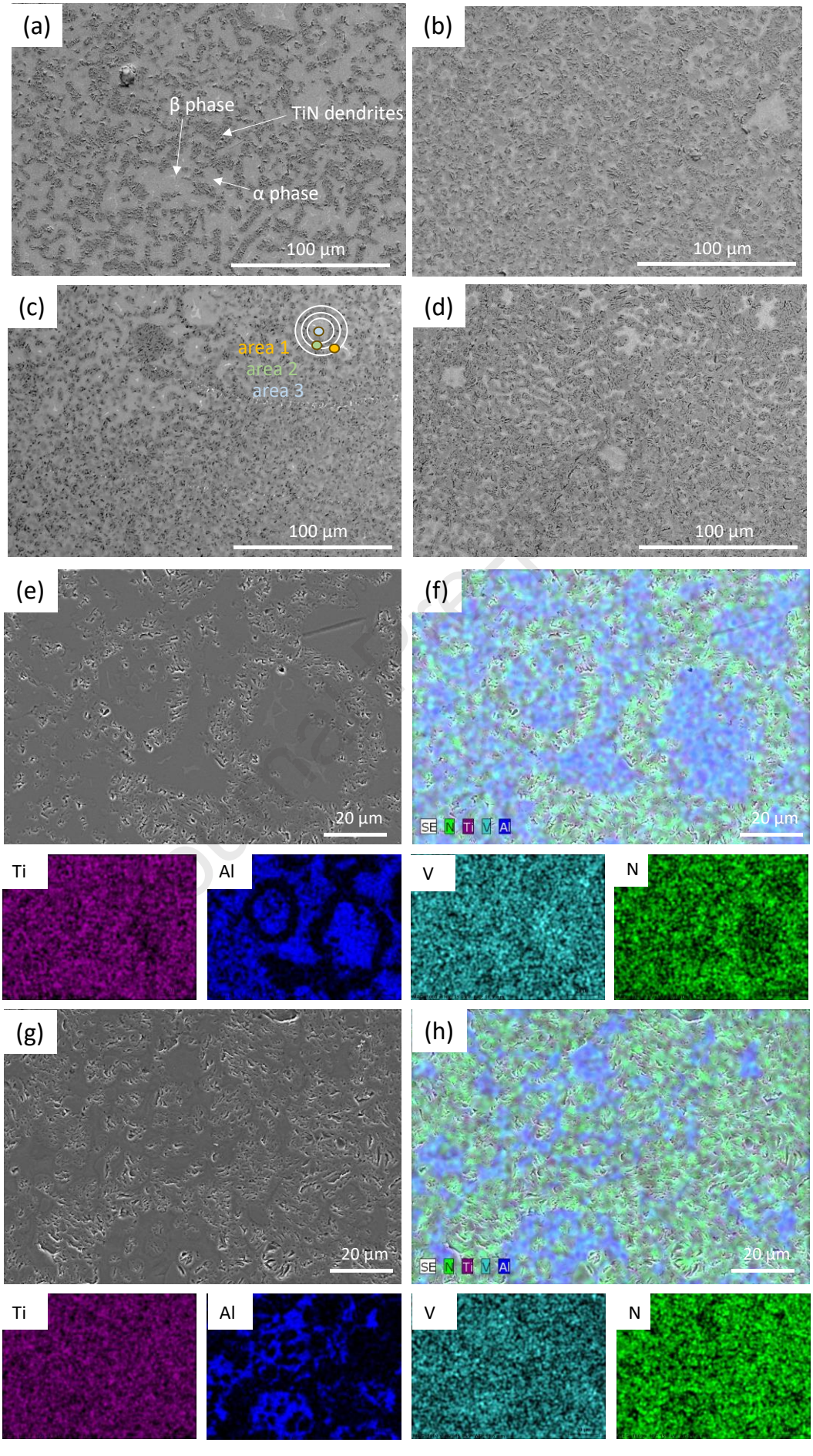
(a)
β phase
TiN dendrites
α phase
100 μm
(b)
100 μm
(c)
area 1
area 2
area 3
100 μm
(d)
100 μm
(e)
20 μm
(f)
SE N Ti V Al
20 μm
Ti
Al
V
N
(g)
20 μm
(h)
SE N Ti V Al
20 μm
Ti
Al
V
N

263

Figure 3. SEM micrographs of the Ti–TiN microstructures in the top region of the cross sections corresponding to heat inputs of (a) 37.5, (b) 75, (c) 95, and (d) 190 J/mm; (e) detailed microstructure and (f) EDX mapping of the 37.5 J/mm sample; (g) detailed microstructure and (h) EDX mapping of the 75 J/mm sample.

3.2. **Microhardness, coefficient of friction, and wear rate**

The data presented in Figure 4 were plotted to evaluate the observed trends not only as a function of heat input but also to separately analyze the effects of power and scanning speed. This distinction was made because these parameters influenced the hardness, CoF, mass loss, and wear rate of the analyzed samples in different proportions.

The Vickers hardness of all the analyzed materials manufactured with argon (Ti, red) and with nitrogen (Ti/TiN, black) is plotted in Figure 4a as a function of the heat input (J/mm) for low (650 W) and high (1200 W) laser power and low (5 mm/s) and high (10 mm/s) scanning speed. The figure shows similar trends (increasing or decreasing) observed when increasing speed at constant power (650 W or 1200 W).

In general, the variation in the microhardness of the unreinforced Ti6Al4V materials was not very significant. However, at equal power, a slight decrease in the microhardness was observed with decreasing scanning speed due to the modification of the Widmanstätten alpha–beta microstructure into wider lamellar grains, as confirmed by the phase width measurements in Figure 2. Therefore, the finest microstructure was obtained at the lowest heat input (37.5 J/mm), and, since these structures are associated with a higher density of grain boundaries that acted as effective barriers to dislocation motion and impeded plastic deformation, their measured hardness was higher. Nevertheless, as the heat input increased (75 J/mm), the thermal gradients decreased and cooling rates were reduced, leading to coarser microstructures (thickening of the alpha phase and an increase in the interlamellar spacing or beta phase).

Figure 4b represents the CoF measured during the wear tests as a function of the heat input and manufacturing parameters. The unreinforced titanium materials exhibited a CoF that, for the same power, increased with increasing laser scanning speed. This could be associated with higher debris generation (to be studied later) because of the high hardness of the material, which could reduce the contact surface and increase the effective load on the contacts during the wear test.

Figures 4c–e represent the pin mass loss, wear rate, and counterbody mass loss after the tests, respectively. A large difference was observed in the mass loss of the reinforced and unreinforced specimens, especially at higher heat input, with the latter losing the most mass (approximately 5 times more; Figure 4c). At low power (650 W), an increase

in speed decreased the pin mass losses, while at high power (1200 W), it remained invariant with speed. The wear rate followed the same trend as the pin mass loss plot (Figure 4d). The values reached a maximum of 2.50×10^{-12} m^3/Nm when the Ti sample was fabricated with a heat input of 95 J/mm (1200 W and 10 mm/s) and remained at similar levels for 190 J/mm (1200 W and 5 mm/s), which is associated with higher mass losses from pins with lower hardness. The wear rate of Ti was up to 5 times higher than that of the composites when the heat input was high, while at low heat input they were practically similar, which is associated with microstructural changes. The mass loss of the counterbodies with which the Ti and Ti/TiN samples were tested (Figure 4e) presented the same evolution profile with the heat input. The losses of the counterbodies tested with unreinforced titanium correlate with the microhardness values: the lower the heat input, the higher the microhardness and counterbody mass loss, and the lower the pin mass loss. All this could lead to a change in the wear mechanism. The adhesive-type wear mechanism could be the most relevant in these cases, since the irregularities of both surfaces would interact at high pressures, resulting in plastic deformation and adhesions by microwelding at contact points.

Thus, in unreinforced titanium materials, two effects were identified in relation to wear rate values: (a) hardness and (b) debris generation. The lower the heat input, the higher the hardness and the lower the pin mass loss and wear rate of the unreinforced material. In turn, the harder pin could generate a greater number of debris from the 316L counterbody, which lost more mass.

The microhardness of the Ti/TiN composites (Figure 4a) followed a decreasing trend with increasing speed for the same power and was double that of the nonreinforced samples due to the formation of in situ TiN dendrites that hardened the titanium matrix. The highest values (1300 HV2) were measured in the samples fabricated at lower laser power and scanning speed (75 J/mm condition). In these samples, the distribution of the reinforcement within the matrix was more homogeneous, which favored high microhardness values. In addition, this was related to two factors: (i) laser scanning speed: the lower the speed, the higher the level of nitriding in the samples, given the longer reaction time of molten titanium with atmospheric nitrogen to form TiN reinforcement in situ, resulting in a higher amount of TiN reinforcement and higher microhardness; and (ii) laser beam power: by decreasing the power, the thickening effect of TiN dendrites as a result of annealing was minimized, resulting in increased microhardness in the composites.

The Ti/TiN samples presented a higher CoF than unreinforced Ti, and both graphs exhibited a similar trend (Figure 4b). The hardening of the matrix by solid solution and generation of nitrides occurred when fabrication took place in a reactive nitrogen atmosphere, which increased both the hardness and CoF of the composite. Other authors have studied the same relationship between CoF and microhardness by

reinforcing metallic materials with ceramics [31]. The CoF of Ti–TiN ranged between 0.7 and 0.9, which is characteristic of materials reinforced with TiN [32]. The 95 J/mm sample exhibited the highest CoF, while the 190 J/mm sample exhibited the lowest, specifically a factor of 1.30 lower, when both samples were fabricated using 1200 W but at different speeds of 10 and 5 mm/s, respectively. For the same laser power, a decrease in the laser scanning speed led to a lower CoF, which cannot be correlated with the hardness variation of these materials but is likely associated with a higher debris generation of the 316L counterbody and thus a change in the wear mechanism. The low CoF for the higher heat input suggests that a mechanically mixed layer (MML) may have formed on the surface, decreasing the mass loss of the sample after the wear test.

For the TiN-reinforced composites, the mass losses were quite low, except for the sample fabricated at 75 J/mm, which presented higher mass loss than the rest of the materials, despite its higher hardness (Figure 4c). As previously mentioned, the laser power and scanning speed had different effects on the distribution of TiN and Ti_2N ceramic reinforcements formed within the Ti6Al4V matrix. The 75 J/mm sample (low scanning speed and low laser power) showed more intense XRD peaks corresponding to nitride phases compared to the 37.5 J/mm sample manufactured with the same laser power (650 W) and higher scanning speed (10 mm/s). Thus, a higher ceramic reinforcement content within the α + β titanium matrix is associated with a higher intrinsic brittleness. This favored fracture mechanisms in the composite sample due to friction against the 316L counterbody, since TiN promoted the formation of microcracks under cyclic contact loading. Therefore, the combination of fabrication parameters (650 W, 5 mm/s) that resulted in samples with a higher proportion of nitrides and increased hardness did not necessarily correlate with enhanced wear resistance (Figure 4d).

Consequently, the counterbody tested with the 75 J/mm Ti/TiN material experienced more damage, resulting in greater material loss compared to the other samples (Figure 4e). A high number of debris from the 316L steel counterbody would increase the local contact load, which would favor the fracture mechanisms of the composite material.

The correlation between the distribution and proportion of TiN and Ti_2N ceramic reinforcement in the metal matrix and the mechanical and tribological factors was studied. On the one hand, an increase in the TiN phase proportion led to a restriction in the plastic deformation of the surrounding titanium matrix and the consequent predominance of abrasive and delamination wear mechanisms. This phenomenon is attributed to the increased generation of hard debris (primarily originating from delamination of the counterbody), acting as third-body abrasives and promoting microcrack initiation and propagation at the matrix–reinforcement interfaces, especially under repeated contact stresses, leading to material loss. Therefore, a laser scanning speed of 10 mm/s (37.5 and 95 J/mm) contributed significantly to minimizing the wear rates of the material under frictional conditions. This higher manufacturing speed

resulted in a reduced nitriding extent of the titanium matrix, thereby limiting the excessive formation of brittle TiN ceramic phases. Consequently, the matrix retained a more balanced microstructure with improved toughness and decreased hardness. Additionally, higher laser scanning speeds are associated with faster solidification rates and steeper thermal gradients, which promote the formation of finer microstructures and can limit the growth of undesirable intermetallic or ceramic phases, thereby enhancing the mechanical integrity of the composite and improving its tribological performance. On the other hand, the higher formation of Ti_2N at the matrix–reinforcement interface in the 95 J/mm sample enhanced the wear performance of these composite materials due to better adhesion of the reinforcing phase to the titanium matrix (higher toughness), reducing crack propagation and the rate of material removal.

Journal Pre-proof

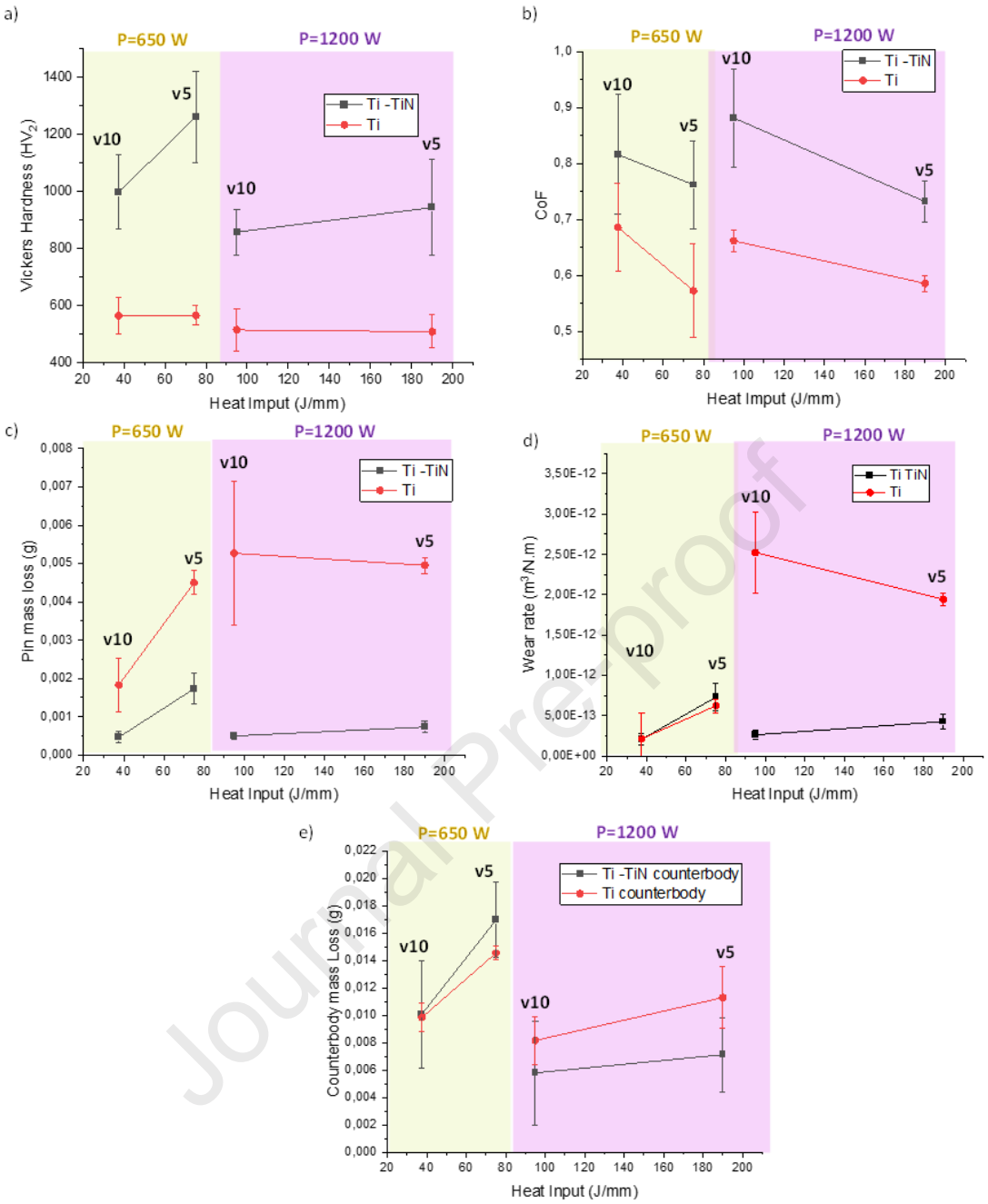

Figure 4. (a) Vickers hardness (HV2), (b) CoF, (c) pin mass loss, (d) wear rate (m^3/Nm), and (e) counterbody mass loss of Ti and in situ Ti/TiN samples manufactured by L-DED.

3.3. Wear mechanisms

The worn surfaces of the Ti pin and disc manufactured with different heat input are shown in Figure 5a, and the generated debris in Figure 5b. Every sample presented furrows of different depths parallel to the sliding direction. Thus, they all experienced abrasion to varying extents, which was the main mechanism in all cases.

When subjected to wear, 37.5 J/mm unreinforced titanium samples (low heat input) suffered plastic deformation in the sliding direction due to the pin–disc friction, leaving

a higher surface roughness with gaps (Figure 5a (1)). Apart from this, its corresponding counterbody exhibited delamination of material fragments and parallel grooves due to surface abrasion (Figure 5a (2)). These laminar-shaped delaminated fragments from the counterbody (Figure 5b (i)) microwelded to the abraded plough grooves of the pin, resulting in a predominantly adhesive wear mechanism.

The 75 J/mm titanium samples exhibited scratches on the pin surface that also led to asperities and parallel grooves formed by debris particles (Figure 5a (3)). Once again, material removal from the 316L counterbody occurred, and the Ti surface became covered with debris adhered through microwelding, which corresponds with the plastic deformation and grooves observed on the counterbody (Figure 5a (4)). This indicates that adhesive wear occurred alongside abrasive wear.

For 95 J/mm samples, slight differences were observed. As previously mentioned, since the titanium material was softer, less debris was detached from the counterbody, resulting in smaller and fewer particles (Figure 5b (iii)), which caused less damage to the pin surface (Figure 5a (5)). This frictional process with the generated debris reduced the contact area and led to abrasive wear, causing significant fluctuations in the CoF [33]. The counterbody again exhibited plastic deformation, and the released debris agglomerated and became trapped in the surface cracks, leading to the formation of small grooves on the wear track, as shown in Figure 5a (6).

Lastly, for 190 J/mm samples (highest heat input), similar characteristics to the previous sample were observed. Wear produced parallel abrasive marks, aligned with the sliding direction (Figure 5a (7)). The corresponding counterbody (Figure 5a (8)) displayed a scratched surface characteristic of abrasion, suggesting a three-body abrasive wear mechanism.

Figure 5b illustrates the wear debris generated during the wear tests. The size and morphology of the debris varied for each material studied. At low heat inputs (37.5 and 75 J/mm), large, flat laminar fragments were identified, likely originating from predominant delamination caused by adhesive wear, corresponding to a higher CoF (Figures 5b (i) and (ii)). Additionally, smaller particles from abrasive wear were observed. At higher heat inputs (95 and 190 J/mm), fragmented chips and smaller particles were detected, associated with three-body abrasive wear (Figures 5b (iii) and (iv)), and corresponding to a lower CoF.

Subsequently, backscattered electron (BSE) images of the wear surfaces of titanium samples fabricated with low (Figure 5c) and high energy (Figure 5d) are shown. Darker particles, resulting from the detachment of debris due to abrasive wear, were identified on both surfaces. For the low-heat input sample, lighter areas were observed where 316L steel adhered to the worn surface (Figure 5c).

Figures 5e–f display the SEM micrographs and corresponding EDX elemental mapping of worn surfaces from unreinforced titanium. The worn surfaces of samples fabricated with the lowest heat input (37.5 J/mm; Figure 5e) showed plastic deformation and indentations caused by heat generated during the friction process between the pin and counterbody. This promoted oxidation, leading to the formation of iron oxides. Iron particles were transferred from the counterbody to the pin, adhering to the surface through microwelding and increasing the iron content on the titanium surfaces, as confirmed by EDX elemental mapping. Figure 5d shows the worn surfaces of titanium samples fabricated with the highest heat input (190 J/mm). The formation of small, abrasive debris was more evident in this case, acting as a third body in the wear process and producing surface abrasion without the influence of adhesive wear. Elemental analysis confirmed that this debris was composed of iron oxides, likely originating from the counterbody, which oxidized due to friction. The oxide particles blocked direct contact between the pin and counterbody, reducing adhesive wear and increasing abrasive wear.

Figure 5g shows the percentage of oxygen and iron determined from the elemental analysis on the worn titanium samples. The oxygen and iron percentages in the titanium samples increased with heat input and correlated with the CoF trend. At low heat input, the adhesive wear mechanism was dominant, and the iron and oxygen contents were high, indicating that the debris consisted of iron oxides. In contrast, at high energy, the abrasive wear mechanism was dominant, and the quantity of these elements decreased.

In summary, titanium fabricated at low power (heat inputs of 37.5 and 75 J/mm) exhibited a wear mechanism that was partly abrasive but primarily adhesive and oxidative, which corresponds to the higher hardness and greater debris accumulation observed on their surfaces. However, for titanium fabricated at high power (heat inputs of 95 and 190 J/mm), the wear mechanism was identified as abrasive, with more pronounced grooves parallel to the wear direction, which is associated with lower hardness.

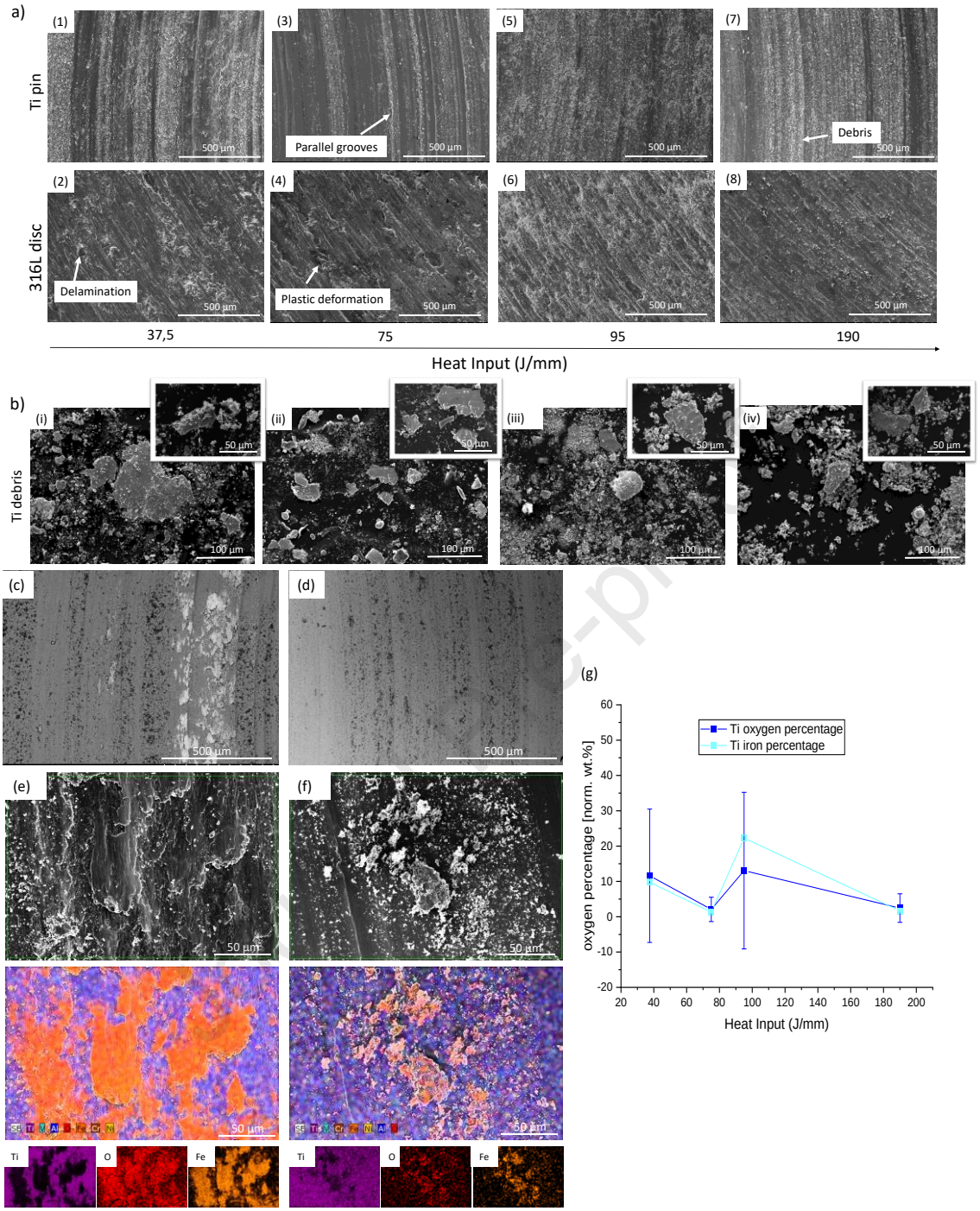

Figure 5. (a) SEM micrographs of the wear surfaces of titanium and their corresponding counterbodies as a function of heat input: (1) and (2) 37.5 J/mm; (3) and (4) 75 J/mm; (5) and (6) 95 J/mm; (7) and (8) 190 J/mm. (b) SEM micrographs of the wear debris resulting from the different wear tests for titanium: (i) 37.5 J/mm; (ii) 75 J/mm; (iii) 95 J/mm; (iv) 190 J/mm. BSE images of the 316L counterbody for (c) low (37.5 J/mm) and (d) high (190 J/mm) heat inputs; detailed view and elemental mapping of the wear surfaces of titanium fabricated at (e) 37.5 J/mm and (f) 190 J/mm; (g) percentage values obtained from the EDX elemental analysis.

The worn surfaces of the Ti/TiN samples and their corresponding counterbodies are shown in Figure 6a as a function of heat input. Abrasion of the wear-exposed surface occurred in all Ti/TiN samples, leaving grooves aligned with the sliding direction.

The 37.5 J/mm Ti/TiN samples (Figure 6a (1)) exhibited plastic deformation and surface abrasion. Clusters of debris were found on the worn surfaces, originating from the counterbody through its delamination. These tended to agglomerate in the indentations formed on the surface of the material (by adhesion) after plastic deformation due to frictional pressure, leading to the extrusion of 316L steel into the material itself. The counterbody exhibited plastic deformation, as well as grooves (Figure 6a (2)). These results correspond to both adhesive and delamination wear mechanisms.

The worn surfaces of 75 J/mm Ti/TiN (Figure 6a (3)) showed slight differences, as they were more fragmented. Delamination of parts of the counterbody occurred, leading to deep indentations and abrasion marks (Figure 6a (4)). These delaminated fragments caused cracking in the ceramic (as it is a composite with high hardness), with cracks propagating until the material fractured, resulting in the highest mass loss for both the pin and counterbody. This resulted in a higher wear rate and a delamination-driven abrasive wear mechanism.

The worn surface of 95 J/mm TiN exhibited shallow grooves, debris adhesion from the counterbody, and plastic deformation (Figure 6a (5)). The wear rate for this sample was among the lowest, along with 37.5 J/mm TiN, which is also associated with lower microhardness and led to an adhesive wear mechanism. This can be explained by changes in the material microstructure: the higher the heat input, the poorer the distribution of the TiN dendrites. Therefore, in this case, greater plastic deformation and shallower abrasion marks were observed, with no severe delamination. The corresponding counterbody showed signs of transferred material, which also tended to agglomerate (Figure 6a (6)).

Figure 6a (7) shows the worn surfaces of the 190 J/mm Ti/TiN sample. Similar to the 75 J/mm sample, the wear mechanism was predominantly abrasive. In this case, an adhesive/oxidative mechanism was also present, as frictional heat promoted the oxidation of the adhered material, forming an MML composed of various oxides, which increased the oxygen content in the sample. The formation of this oxide tribolayer is associated with a lower CoF due to the lubricating effect. The oxide debris covered composite surfaces, which simultaneously underwent plastic deformation. Figure 6a (8) shows the worn surface of the corresponding counterbody. Surface scratching occurred due to abrasion, and small abrasive debris particles covered the worn surface, more so than in the other counterbodies. The mass loss of this counterbody was relatively low, as no fractures were identified in the material, and small abrasive debris particles,

originating from the collapse of the MML, adhered to the surface, offsetting the mass losses.

The debris generated in the wear tests of the Ti/TiN samples is shown in Figure 6b. The debris from the 37.5 and 95 J/mm samples exhibited a similar appearance following the adhesive wear mechanism, where large clusters of agglomerated oxides and delaminated fragments formed (Figures 6b (i) and (iii)). In contrast, the debris from 75 J/mm (Figure 6b (ii)) and 190 J/mm Ti/TiN samples (Figure 6b (iv)) revealed small particles typical of abrasive wear. Additionally, the 190 J/mm sample showed more fractured particles characteristic of adhesive wear, composed in some cases of oxide clusters and in others of small, delaminated material flakes (possibly oxidized, as they likely originated from the formed MML).

The BSE SEM images of the worn surfaces of the pins fabricated with low (75 J/mm) and high (190 J/mm) heat input are shown in Figures 6c and 6d, respectively. These micrographs revealed greater adhesion of material from the 316L counterbody in the sample fabricated with higher energy, which correlates with lower hardness and CoF.
The EDX elemental analysis maps performed on the worn surfaces of the Ti/TiN samples fabricated at low and high heat input are shown in Figures 6e and 6f, respectively. The measured oxygen, iron, and nitrogen contents are represented in Figure 6g. The EDX results of the 75 J/mm TiN sample showed clusters of debris consisting of aggregated iron and oxygen across the entire worn surface. On the other hand, the 190 J/mm Ti/TiN sample exhibited an MML also composed of iron oxides that covered its surface. The micrographs indicate that this layer was much denser than the oxides formed at low heat input, corresponding to the higher percentage of iron and oxygen measured in the 190 J/mm pin (Figure 6g). Therefore, higher laser power and lower scanning speeds (i.e., higher heat input), combined with in situ introduction of TiN reinforcement using nitrogen, led to increased iron oxide formation. In general, iron oxide clusters and the MML covered both the titanium matrix and TiN reinforcement; therefore, nitrogen and titanium were only detected in areas where there were no agglomerations or where the MML fractured, indicating that iron oxides, rather than titanium oxides, were formed. The MML acted as a solid lubricant, reducing the direct contact between the matrix and counterbody, and thus partially mitigating the otherwise dominant abrasive mechanisms.

In summary, the Ti/TiN samples fabricated at faster laser scanning speeds (heat inputs of 37.5 and 95 J/mm) exhibited a predominantly adhesive wear mechanism, characterized by the formation of a metallic transfer layer on the worn surfaces. This is attributed to increased plastic deformation and the relatively ductile behavior of the titanium-rich matrix. Here, rapid solidification limited the extent of the titanium nitriding reaction, resulting in a reduced volume fraction of TiN and a correspondingly lower overall hardness of the composite. Moreover, the formation of Ti_2N—particularly

evident in samples fabricated at higher power (e.g., 95 J/mm)—was found to improve the matrix–reinforcement interface stability and mitigate crack propagation, contributing to structural integrity during sliding. Conversely, at slower scanning speeds (heat inputs of 75 and 190 J/mm), the longer laser-material interaction time enhanced the nitriding reaction and promoted the formation of larger proportions of brittle TiN ceramic phases with higher hardness, which facilitated surface fragmentation and increased susceptibility to abrasive and delamination wear mechanisms. An exception was observed in the sample fabricated under the highest heat input (190 J/mm). Despite the high TiN content, this sample exhibited a predominantly adhesive/oxidative wear behavior, attributed to the development of a stable tribolayer (MML), composed primarily of iron oxides transferred from the steel counterbody, which acted as a lubricant and mitigated the abrasive wear mechanism.

Journal Pre-proof

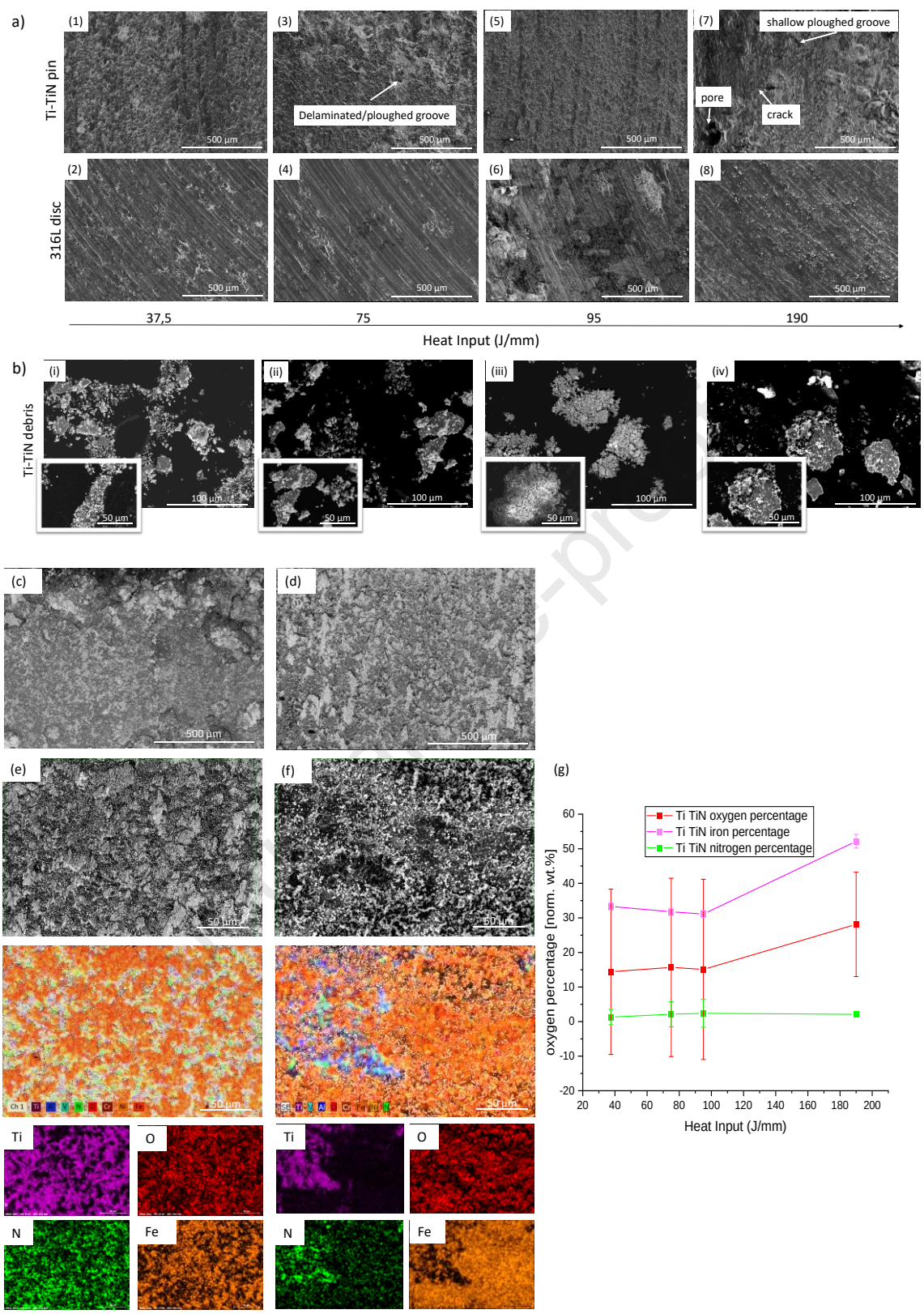

Figure 6. (a) SEM micrographs of the worn surfaces of Ti/TiN and their corresponding counterbodies as a function of the heat input: (1) and (2) 37.5 J/mm; (3) and (4) 75 J/mm; (5) and (6) 95 J/mm; (7) and (8) 190 J/mm. (b) SEM micrographs of the debris generated from the wear tests for Ti/TiN: (i) 37.5 J/mm; (ii) 75 J/mm; (iii) 95 J/mm; (iv) 190 J/mm. BSE image of the 316L counterbody for (c) low (75 J/mm) and (d) high (190 J/mm) heat inputs; detailed view and

Journal Pre-proof

elemental mapping of the worn surfaces of Ti/TiN fabricated at (e) 75 J/mm and (f) 190 J/mm; (g) percentage values obtained from the EDX elemental analysis.

4. Conclusions

The wear behaviors of L-DED additively manufactured Ti6Al4V/TiN composite materials and unreinforced titanium samples, fabricated using varying laser powers and scanning speeds, were analyzed. Heat input values were calculated based on the processing parameters. Their microstructure was analyzed and correlated with their Vickers microhardness, wear rate, CoF, pin and disc mass losses, and wear mechanisms.

- All the unreinforced titanium samples exhibited a Widmanstätten alpha–beta titanium microstructure regardless of heat input, which evolved into a wider lamellar structure as heat input increased. The titanium composites showed an alpha–beta titanium matrix with in situ TiN and Ti_2N dendrites formed from the nitrogen–titanium reaction.
- Vickers microhardness of Ti/TiN composites was twice that of the unreinforced samples, and the trend increased at lower scanning speeds for the same laser power due to a greater nitriding effect. The maximum microhardness was 1300 HV2 and corresponds to the 75 J/mm Ti/TiN sample.
- The CoF was higher for the Ti/TiN samples. A 1.30× difference was measured between the highest CoF (95 J/mm) and the lowest (190 J/mm), which is attributed to the formation of an MML on the surface of the latter and a corresponding change in the dominant wear mechanism.
- The formation of the TiN reinforcement phase in the composite samples led to lower wear rates. The minimum wear rate measured was 2.5×10^{-13} m^3/Nm for the 37.5 and 95 J/mm Ti/TiN samples owing to a lower proportion (lower brittleness) and better distribution of TiN reinforcements.
- The fracture mechanisms of the 75 J/mm Ti/TiN sample were promoted owing to having the highest hardness, facilitating the removal of material from the counterbody, and resulting in the most mass loss due to embrittlement from the debris effect of the counterbody.
- The abrasive wear mechanism was present in all samples, and plastic deformation occurred in all counterbodies. For the Ti samples, lower power corresponds to a greater contribution of delamination and adhesive/oxidative wear mechanisms, while higher power corresponds to a greater contribution from abrasive mechanisms.
- For Ti/TiN composite materials, higher laser scanning speeds correspond to a greater contribution of the adhesive wear mechanism, while slower scanning speeds favored the abrasive wear mechanism, with an additional adhesive/oxidative component for the 190 J/mm sample due to the formation of an MML.

Acknowledgements

Funding: This work was supported by the Agencia Estatal de Investigación (projects PID2021-124341OB-C21, TED2021-129849B-I00, PLEC2023-010346).

References

[1] A. Aversa, A. Saboori, E. Librera, M. de Chirico, S. Biamino, M. Lombardi, P. Fino, The role of Directed Energy Deposition atmosphere mode on the microstructure and mechanical properties of 316L samples, Addit. Manuf. 34 (2020) 101274. https://doi.org/10.1016/j.addma.2020.101274.

[2] G. Rasiya, A. Shukla, K. Saran, Additive Manufacturing-A Review, Mater. Today Proc. (2021). https://doi.org/10.1016/j.matpr.2021.05.181.

[3] S.M. Thompson, L. Bian, N. Shamsaei, A. Yadollahi, An overview of Direct Laser Deposition for additive manufacturing; Part I: Transport phenomena, modeling and diagnostics, Addit. Manuf. 8 (2015) 36–62. https://doi.org/10.1016/j.addma.2015.07.001.

[4] B.E. Carroll, A. Palmer, A.M. Beese, ScienceDirect Anisotropic tensile behavior of Ti – 6Al – 4V components fabricated with directed energy deposition additive manufacturing, Acta Mater. 87 (2015) 309–320. https://doi.org/10.1016/j.actamat.2014.12.054.

[5] M.J.J.A.J. Danovitch, Y.T.M. Brochu, Additive Manufacturing of AlSi10Mg Alloy Using Direct Energy Deposition : Microstructure and Hardness Characterization, J. Therm. Spray Technol. 26 (2017) 587–597. https://doi.org/10.1007/s11666-016-0495-4.

[6] C. Zeng, H. Wen, H. Bellamy, P.T. Sprunger, P.J. Schilling, S.M. Guo, Titanium and nitrogen interactions under laser additive manufacturing conditions, Surf. Coatings Technol. 378 (2019) 124955. https://doi.org/10.1016/j.surfcoat.2019.124955.

[7] C.S. de Rojas Candela, A. Riquelme, P. Rodrigo, J. Rams, Carrying Gas Influence and Fabrication Parameters Impact in 3D Manufacturing of In Situ TiN-Ti Composites by Direct Laser Deposition, Met. Mater. Int. 29 (2023) 591–606. https://doi.org/10.1007/s12540-022-01260-2.

[8] B. Shi, S. Huang, P. Zhu, C. Xu, P. Guo, Y. Fu, In-situ TiN reinforced composite coatings prepared by plasma spray welding on Ti6Al4V, Mater. Lett. 276 (2020) 128093. https://doi.org/10.1016/j.matlet.2020.128093.

[9] N. Singh, P. Hameed, R. Ummethala, G. Manivasagam, K.G. Prashanth, J. Eckert, Selective laser manufacturing of Ti-based alloys and composites: impact of process parameters, application trends, and future prospects, Mater. Today Adv. 8 (2020) 100097. https://doi.org/10.1016/j.mtadv.2020.100097.

[10] A.F. Erica Liverani, Stefania Toschi, Lorella Ceschini, Effect of Selective Laser Melting (SLM) process parameters on microstructure and mechanical properties of 316L austenitic stainless steel, (2017). 10.1016/j.jmatprotec.2017.05.042.

[11] C.S. de Rojas Candela, A. Riquelme, V. Bonache, P. Rodrigo, J. Rams, Ti6Al4V/SiC Metal Matrix Composites Additively Manufactured by Direct Laser Deposition,

Met. Mater. Int. (2022). https://doi.org/10.1007/s12540-022-01191-y.
[12] R.M. Mahamood, E.T. Akinlabi, Heat affected zone Relationship with processing parameter in Additive Manufacturing Process, Mater. Today Proc. 5 (2018) 18362–18367. https://doi.org/10.1016/j.matpr.2018.06.175.
[13] A. Riquelme, C. Sánchez de Rojas Candela, P. Rodrigo, J. Rams, Influence of process parameters in additive manufacturing of highly reinforced 316L / SiCp composites, J. Mater. Process. Technol. 299 (2022). https://doi.org/10.1016/j.jmatprotec.2021.117325.
[14] A. Riquelme, P. Rodrigo, M.D. Escalera-Rodriguez, J. Rams, Effect of the process parameters in the additive manufacturing of in situ Al/AlN samples, J. Manuf. Process. (2019). https://doi.org/10.1016/j.jmapro.2019.09.011.
[15] Y. Liu, Z. Chen, J. He, Nanosized SiC particle reinforced Ti6Al4V matrix composites manufactured by laser melting deposition, Procedia Struct. Integr. 42 (2022) 1249–1258. https://doi.org/10.1016/j.prostr.2022.12.159.
[16] K.U. Kainer, Basics of Metal Matrix Composites, in: Met. Matrix Compos. Cust. Mater. Automot. Aerosp. Eng., 2006. https://doi.org/10.1002/3527608117.ch1.
[17] A. Kumar, O. Vichare, K. Debnath, M. Paswan, Fabrication methods of metal matrix composites (MMCs), Mater. Today Proc. 46 (2020) 6840–6846. https://doi.org/10.1016/j.matpr.2021.04.432.
[18] C. Zhong, J. Liu, T. Zhao, T. Schopphoven, J. Fu, A. Gasser, J.H. Schleifenbaum, Laser metal deposition of Ti6Al4V-A brief review, Appl. Sci. 10 (2020) 1–12. https://doi.org/10.3390/app10030764.
[19] F. Bartolomeu, M.M. Costa, N. Alves, G. Miranda, F.S. Silva, Additive manufacturing of NiTi-Ti6Al4V multi-material cellular structures targeting orthopedic implants, Opt. Lasers Eng. 134 (2020) 106208. https://doi.org/10.1016/j.optlaseng.2020.106208.
[20] I.A. Ibrahim, F.A. Mohamed, E.J. Lavernia, Particulate reinforced metal matrix composites - a review, J. Mater. Sci. (1991). https://doi.org/10.1007/BF00544448.
[21] Y. Sahin, The prediction of wear resistance model for the metal matrix composites, Wear. 258 (2005) 1717–1722. https://doi.org/10.1016/j.wear.2004.11.024.
[22] F. Pougoum, T. Schmitt, L. Martinu, J.E. Klemberg-Sapieha, S. Savoie, R. Schulz, Wear behavior of Fe3Al-TiN-TiB2 HVOF coatings: A comparative study between in situ and ex situ powder processing routes, Ceram. Int. 43 (2017) 8040–8050. https://doi.org/10.1016/j.ceramint.2017.03.122.
[23] R.T. Dispersoids, J. Umeda, H. Fujii, R. Takizawa, T. Teramae, A. Issariyapat, S. Kariya, Y. Yang, S. Li, K. Kondoh, Tribological Behavior of Titanium-Sintered Composites with, (2022).
[24] C. Song, M. Liu, Z.Q. Deng, S.P. Niu, C.M. Deng, H.L. Liao, A novel method for in-situ synthesized TiN coatings by plasma spray-physical vapor deposition, Mater. Lett. 217 (2018) 127–130. https://doi.org/10.1016/j.matlet.2018.01.068.
[25] W. Wei, W. Wu, S. Fan, X. Duan, In-situ laser additive manufacturing of Ti6Al4V matrix composites by gas–liquid reaction in dilute nitrogen gas atmospheres, Mater. Des. 202 (2021) 109578. https://doi.org/10.1016/j.matdes.2021.109578.
[26] B. AlMangour, D. Grzesiak, J.M. Yang, In-situ formation of novel TiC-particle-reinforced 316L stainless steel bulk-form composites by selective laser melting, J.

Alloys Compd. 706 (2017) 409–418. https://doi.org/10.1016/j.jallcom.2017.01.149.

[27] J.K. Lancaster, The influence of substrate hardness on the formation and endurance of molybdenum disulphide films, Wear. (1967). https://doi.org/10.1016/0043-1648(67)90082-8.

[28] W. Messler, Principles of welding. Processes, Physics, Chemistry and Metallurgy, Wiley-VCH, 2004.

[29] G. Kaya, F. Yıldız, İ.H. Korkmaz, İ. Kaymaz, A.F. Yetim, T.O. Ergüder, Ç. Şen, Effects of process parameters on selective laser melting of Ti6Al4V-ELI alloy and parameter optimization via response surface method, Mater. Sci. Eng. A. 885 (2023). https://doi.org/10.1016/j.msea.2023.145581.

[30] Afsaneh Edrisy and Khorameh Farokhzadeh, Plasma Science and Technology - Progress in Physical States and Chemical Reactions, in: Plasma Nitriding Titan. Alloy., 2016. https://doi.org/10.5772/61937.

[31] Y. Zhao, T. Yu, C. Guan, J. Sun, X. Tan, Microstructure and friction coe ffi cient of ceramic (TiC , TiN and B 4 C) reinforced Ni-based coating by laser cladding, Ceram. Int. 45 (2019) 20824–20836. https://doi.org/10.1016/j.ceramint.2019.07.070.

[32] Q. Cheng, P. Zhang, X. Ma, S. Wan, W. Hu, W. Wang, G. Yi, J. Zhao, Microstructure evolution and wear mechanism of in situ prepared Ti – TiN cermet layers at high temperature, Compos. Part B. 242 (2022) 110028. https://doi.org/10.1016/j.compositesb.2022.110028.

[33] Y. Su, F. Jiang, M. Long, F. Wu, Z. Xiao, M. Wu, Tribology International Microstructure and frictional properties of copper-tin composites containing graphite and MoS 2 by rapid hot-press sintering, Tribol. Int. 183 (2023) 108392. https://doi.org/10.1016/j.triboint.2023.108392.

Journal Pre-proof

Declaration of Interest Statement

☒ The authors declare that they have no known competing financial interests or personal relationships that could have appeared to influence the work reported in this paper.

☐ The author is an Editorial Board Member/Editor-in-Chief/Associate Editor/Guest Editor for this journal and was not involved in the editorial review or the decision to publish this article.

☐ The authors declare the following financial interests/personal relationships which may be considered as potential competing interests:

Journal Pre-proof